IEEE Access
Multidisciplinary ⋮ Rapid Review ⋮ Open Access Journal

Received 14 August 2023, accepted 23 August 2023, date of publication 1 September 2023, date of current version 7 September 2023.

Digital Object Identifier 10.1109/ACCESS.2023.3311202

RESEARCH ARTICLE

Lightweight Floating Platform for Ground-Based Emulation of On-Orbit Scenarios

BARIŞ CAN YALÇIN, (Member, IEEE), CAROL MARTINEZ, (Member, IEEE), SOFÍA COLOMA, ERNEST SKRZYPCZYK, AND MIGUEL A. OLIVARES-MENDEZ, (Member, IEEE)

Space Robotics (SpaceR) Research Group, Interdisciplinary Centre for Security, Reliability and Trust (SnT), University of Luxembourg, Campus Kirchberg, L-1855 Luxembourg City, Luxembourg

Corresponding author: Barış Can Yalçın (bariscan.yalcin@uni.lu)

This study has been conducted by SnT-SpaceR under Luxembourg National Research Fund (FNR) - BRIDGES funding for "**H**igh fid**EL**ity t**E**sting e**N**vironment for Active Space Debris Removal - **HELEN**", project ref: BRIDGES2021/MS/15836393.

ABSTRACT Orbital space operations must be executed safely and reliably to prevent unwanted failures. One way to validate these operations on Earth is by using testbed facilities that emulate zero-gravity conditions. This article presents the design and evaluation of a novel lightweight floating platform. The objectives are three-fold; the usage of carbon-fiber material for the mechanical structure of the floating platform; the construction of the software packages, which are based on Robot Operating System (ROS); and the floating platform's position controller synthesis, created using disturbance rejection-based convex optimization method to suppress ground-induced mechanical disturbances and ensure stability. Two types of experiments are conducted in the multi-purpose Zero-G Lab facility of the SnT-University of Luxembourg to validate the performance of the floating platform, 1- Position control (single platform); 2- Emulation of an on-orbit cooperative docking scenario (two platforms). Results validate the use of the floating platform for emulating on-orbit scenarios. Optimized in the frequency domain, the proposed controller gives satisfying results for both disturbance rejection and set-point tracking purposes. The link to the Open-source ROS packages is available in the Appendix-B section.

INDEX TERMS Orbital scenario emulation, orbital robotics, floating platform, pneumatic levitation, robust control.

I. INTRODUCTION

Orbital Servicing, Assembly and Manufacturing (OSAM) and Space Debris Removal (SDR) are becoming important research and commercial activities nowadays. Earth orbits are getting populated by old space assets and the amount of planned missions is increasing strongly in the next years. In addition, there are plans to have several space stations and other large structures in Earth orbits in the next decade to be partially assembled and/or manufactured in space. All these activities are demanding a higher autonomy level and close interaction. In order to ensure safe, secure, and reliable in-orbit operations it is demanded to validate and verify Guidance, Navigation, and Control (GNC) algorithms on the ground before sending the mission to space. Therefore, there is a need to develop convenient experimental setups to test all these algorithms [1].

Different facilities have been created for this purpose [2], [3]. Orbital Robotics and Guidance, Navigation, and Control Lab (ORGL) at European Space Research and Technology Centre (ESTEC) with the European Space Agency (ESA) [4], the Orbital Robotic Interaction, On-orbit servicing, and Navigation Laboratory of Florida Tech [5] (ORION), Autonomous Space-craft Testing of Robotic Operations in Space of Georgia-Tech [6] (ASTROS), Advanced Autonomous Multiple Spacecraft laboratories of University of Florida [7] (ADAMUS) are among the most known ones. These facilities have real-time testing capabilities

The associate editor coordinating the review of this manuscript and approving it for publication was Ton Duc Do.

with high-fidelity equipment, such as robotic manipulators, high sampling speed motion capture systems, and floating platforms. Among this equipment, floating platforms allow us to emulate micro-gravity conditions using its pneumatic levitation principle, providing zero friction on 2D [8].

Floating platforms have pneumatic components mounted beneath the structure called ''air-bearing'', that blow high-pressurized air toward an epoxy floor or a granite table to remove the mechanical contact between the air-bearings and the floor. From this point of view, floating platforms are pneumatically levitated devices. Mock-up of space debris, robotic manipulator, SDR systems, locomotion system, or any hardware can be mounted/assembled on a floating platform [9]. Therefore, floating platforms can be used to verify and validate any space system's motion performance on 2D [10].

Floating platforms operate on granite or epoxy surfaces. However, the micron-scale unevenness of these surfaces generates considerable mechanical disturbance effects, especially for heavyweight floating platforms. When the floating platform's weight increases, the effect of mechanical disturbance caused by the unevenness of the ground is propagated. The SpaceR-SnT's lightweight floating platform provides a structural advantage for the emulation of in-orbit operations compared to other floating platforms in the literature. Moreover, it ensures longer experiment duration since heavy floating platforms consume more air and limit experiment time. In addition to this, the floating platform's position controller is created using convex optimization methods to ensure the suppression of ground-induced mechanical disturbances and the stability of the platform.

This article presents the design and evaluation of SpaceR-SnT's lightweight floating platform. The contributions of this work are three-fold:

- **A lightweight platform**: The floating platform is made of additive manufacturing using carbon-fiber material, which contributes to increasing experiment time (complex scenarios can be emulated) and alleviates problems due to the mechanical disturbance caused by the floor unevenness.
- **Open source software**[1]: The floating platform ROS package enables the control of the platform using MATLAB's official ROS toolbox and the visualization of the experiment in RViz (CAD models are provided). Additionally, we provide the floating platform simulator, which is a Gazebo ROS package. To the author's knowledge, in the state of the art, there is no open-source floating platform environment where researchers can develop control algorithms strategies and contribute to disseminating knowledge in space applications.
- **Position controller**: The well-known Linear Matrix Inequality (LMI) based disturbance rejection controller is used to control the SpaceR-SnT's floating platform. This method has not been used before in this application domain. We provide performance tests for this controller and demonstrate that it suppresses ground-induced mechanical disturbances.

The multipurpose Zero-G Lab facility of the SnT-University of Luxembourg is used to evaluate the performance of the floating platform to emulate on-orbit scenarios [11], [12], [13]. Two scenarios are tested: position control (one floating platform), and cooperative docking (two platforms).

The paper is organized as follows; Section II presents the state of the art. Section III introduces the structure of the floating platform. Section IV describes the system dynamics of the floating platform and the controller approach. Section V explains the open-source packages. Section VI shows the experimental results, and Section VII presents the conclusion.

II. STATE OF THE ART

A. DESIGN AND MATERIALS

Several institutions have developed their own floating platform designs having varying degrees-of-freedom (DoF), shapes, geometries, weights, software and hardware components [8]. National Technical University of Athens (NTUA) has a floating platform, namely NTUA space robot simulator, which is 14 kg [14]. The floating platform of the Space Research Centre of the Polish Academy of Sciences is 66 kg [15]. German Aerospace Center's (DLR) floating platform is 50 kg [16]. Tohoku University's free-floating orbital emulator, namely EFFORTS, is mostly composed of heavy aluminum parts [17]. The weight of the floating platform is a very important factor since it determines the endurance of the floating platform, thus the endurance of the experiments [18], [19]. If the floating platform's weight increases, air-bearings consume more air to compensate for increased weight [16], [20]. For instance, the floating platform of ORGL at ESTEC with ESA is approximately 225 kg, and it can only be moved by a crane when it is not being operated [21]. Floating platforms are mostly made of aluminum, plastic, and 3D printing materials (ABS, PLA, *etc*). The material with the highest weight in most designs is aluminum and its alloys. Even though aluminum may seem to be a good candidate to make a balance between material strength and weight, using this material significantly reduces the whole operation time because of weight [23]. Moreover, other components being added on top of floating platforms also increase weight, such as compact air bottles, electronic components, solenoid valves, sensors, etc. [24], [25]. The existing floating platforms in the literature lack of modularity and lightweight structure. Compared to other existing platforms, the design of the SpaceR-SnT floating platform provides modularity and increases endurance. Its total weight is 10.95 kg when the compact air bottle is full. A comparison in terms of weight for some well-known floating platforms in the literature is given in Fig. 1.

B. CONTROL APPROACHES

Several control approaches are proposed in the literature for the motion control of floating platforms. From classical PID

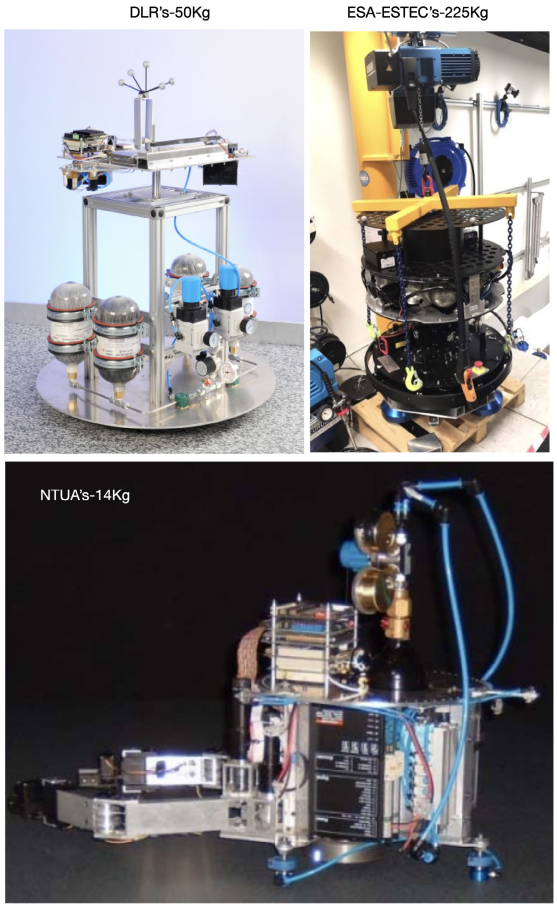

FIGURE 1. Existing floating platforms from DLR 's-50kg [16], ESA-ESTEC's-225kg [21], and NTUA's-14kg [14].

to Linear Quadratic Regulator (LQR) based approaches [26], [27]. The Lyapunov-based nonlinear approach is proposed by [28], [29], and [30]. However, these classical control methods require relatively long trial-and-error steps to reach a good balance of stability and robustness to be compatible with high standards of industrial aspects. At this point, convex optimization-based controllers offer better alternatives since they relatively do not require these steps.

In convex optimization, thrust force (as linked with air consumption) optimization based on Time-Varying Linear Quadratic Regulator (TVLQR) is conducted for a trajectory tracking task, and states are estimated by a Kalman Filter in [21]. Model Predictive Static Programming (MPSP) based on a fast nonlinear optimal control framework is suggested by [31] for trajectory tracking. Stochastic nonlinear optimal control (SNOC) is used in [32] to tackle obstacle avoidance problems in uncertain environments. These methods bring high computational costs, even though they have performed successful and satisfying set-point tracking with stochastic disturbance rejection performance. However, computational simplicity and low delay for motion control of the floating platform are required to emulate on-orbit scenarios, especially in cases where communication with other sub-systems is essential, i.e., any other robotic systems in the network. Because of this, we propose to use a well-known, computationally effective LMI-based approach and experimentally test its performance in this application field.

LMIs representing asymptotic stability and disturbance rejection for motion control are constructed as convex optimization problem and solved in polynomial time by Interior Point Method [33] using open-source SeDuMi solver [34] with YALMIP parser [35]. To construct an advanced optimal robust controller structure for mechanical disturbance attenuation purposes along $[0, \infty)$ stochastic disturbance frequency band, LMI-based controllers are one of the primary choices. Frequency domain optimization methods using LMIs, such as LMI-based infimum and supremum norm minimizations, are helpful because they can suppress a wide range of disturbance frequencies.

The floating platform operates on an epoxy floor, which has micro inclination points creating ground-induced mechanical disturbances. To suppress mechanical disturbance parameters, closed-loop control of air-bearing is not possible since the air gap between the air-bearing and the floor is around 5 microns. Any tiny dust particle may create mechanical disturbance. In this paper, we propose to use a disturbance rejection-oriented closed-loop position controller for the floating platform, which constitutes a very compact, flexible, and computationally low-cost controller, compared to other controllers for floating platforms in the literature. The LMI-based robust controller will be ground/surface-agnostic and can be used on different space laboratories/surfaces.

III. THE SpaceR-SnT FLOATING PLATFORM

The floating platform's components are explicitly given in the following subsections.

A. MECHANICAL COMPONENTS

Fig. 2 presents the CAD of the floating platform. It consists of three geometrically identical dodecagons (12-sided polygon) plates made of string-like carbon-fiber material. This string-like design approach provides the lightweight property with optimal usage of the volume and at the same time mechanical strength due to the physical properties of the carbon-fiber-based additive manufacturing method. The lower plate is fully black, whereas the middle and upper plates have four different colors, grey, blue, red, and white. The colors help to visually identify the orientation of the floating platform during experiments.

The lower plate contains the two main pneumatic components that make the floating platform move, such as nozzles and air-bearings. In total, it has eight nozzles and four air-bearings. Air-bearings make the floating platform cut the mechanical contact with the epoxy floor, whereas nozzles are used to achieve 3-DoF motion. Moreover, the voltage regulator, Raspberry Pi-4B (RPi4B), compact air bottle, power supply, pressure regulators, relay board, and solenoid valves are located on the lower plate given in Fig. 2.

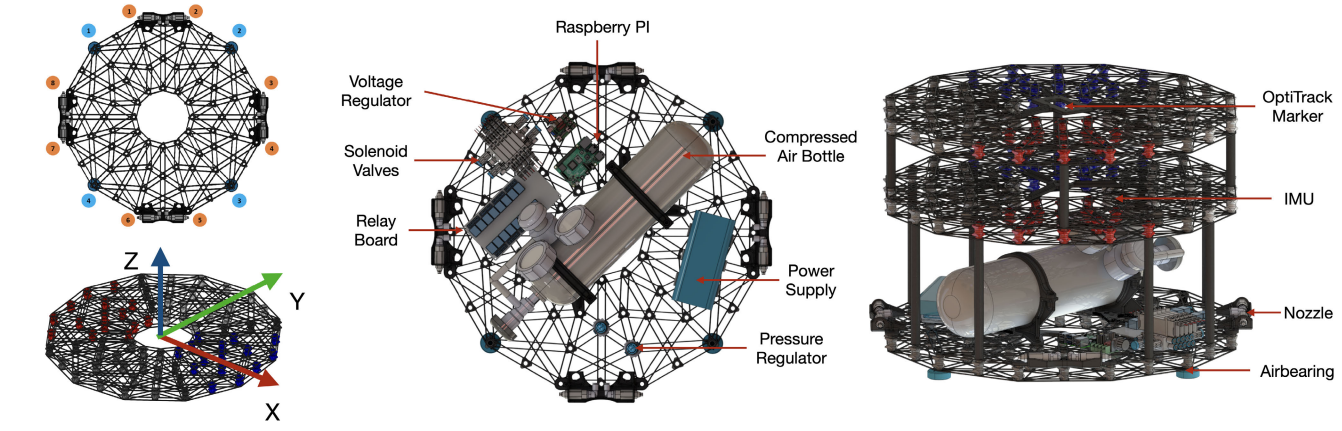

FIGURE 2. SpaceR-SnT Floating platform CAD drawings.

Furthermore, the floating platform's design is modular. The middle and upper plates can easily be disassembled, or used for carrying equipment related to any emulation scenario. String-like topology of the plate structure allows for placing many components. 3D printed supports can easily be integrated into the strings and be used to assemble additional equipment, such as debris removal systems, debris mockups, refueling or docking mockups [37], [38], sensors, etc. Each plate is 60 cm diameter and the distance between the plates is adjustable. Therefore, the floating platform provides an advantage for the implementation of any equipment.

B. PNEUMATIC COMPONENTS

1) AIR-BEARINGS

The plate scheme and the locations of the air-bearings can be seen in the first column of Fig. 2. For the configuration of the air-bearings, the square approach has been used to compensate for the weight distribution of the floating platform in a homogeneous way. The selection criteria for air-bearing is directly related to how much weight the floating platform is, and how much weight it will carry. In the floating platform configuration, 40 mm diameter flat round air-bearing is used, which is capable of lifting a maximum of 22.5 kg if it is actuated by 5 bar. The maximum lifting capacity of four air-bearings together is 90 kg.

2) NOZZLES

The floating platform has eight nozzles to ensure 3-DoF movement. The actuation of the nozzles with a specific configuration drives the floating platform along two translational axes, X and Y, and around one rotational axis Z (yaw). The nozzle locations are given in Fig. 2. The configuration of the nozzles for each specific movement can be seen in Table 1. The nozzles used in the floating platform are FESTO LPZ-SD high-thrust air-jet nozzles. The selection criteria of the nozzle in the floating platform structure are linked to how much force it can generate under different pressure values. This nozzle model can generate 0-1 N force under 0-10 bar. For each DoF, maximum two nozzles are used at the same time since the more nozzles are used the more losses occur.

TABLE 1. Nozzle configuration.

Nozzle	Motion					
#	X^+	X^-	Y^+	Y^-	Z^+	Z^-
1	1	0	0	0	1	0
2	0	1	0	0	0	1
3	0	0	0	1	1	0
4	0	0	1	0	0	1
5	0	1	0	0	1	0
6	1	0	0	0	0	1
7	0	0	1	0	1	0
8	0	0	0	1	0	1

3) SOLENOID VALVES

In this study, FESTO VTUG is used as solenoid valve energized by a 5 V DC. The selection criteria for solenoid valve is linked to pressure constraints of compressed air source, air-bearings, and nozzles. Solenoid valve must ensure appropriate pressure input value for compressed air source and appropriate output pressure value for air-bearings and nozzles.

The solenoid valve configuration of our floating platform is given in Fig 3. Pilot air feeds to the solenoid valves that supply air to air-bearings and nozzle. Four air-bearings in parallel configuration are connected to the solenoid valve-9, and each nozzle is connected to a single solenoid valve, the sequence is Nozzle#n is connected to solenoid valve#n. Solenoid valve#10 is idle since the solenoid valve manifold has ten solenoid valves as standard. The parts shown with red color in Fig. 3 are acoustic silencers. Since solenoid valves have binary logic, they must be modulated to obtain continuous controller output force. The well-known method for this purpose is Pulse-Width Pulse-Frequency (PWPF) modulation. This method uses a dynamic ON-OFF sequence

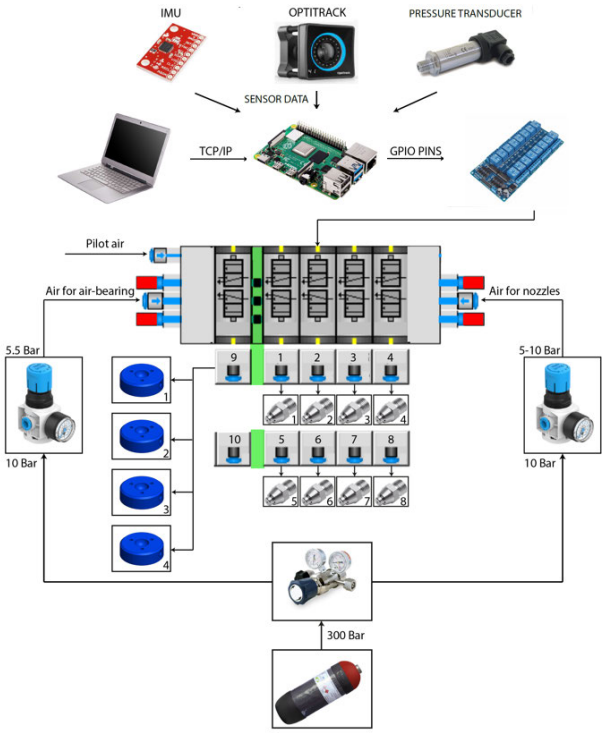

FIGURE 3. Functional diagram.

for the solenoid valves to obtain the equivalent average force by changing the duty cycle of the signal [39]. The condition generates the second selection criteria for the solenoid valve. To obtain a wide range of continuous controller output force, the chosen solenoid valve should be driven between 5-10 Hz frequency using PWPF modulation method.

4) COMPRESSED AIR SOURCE

As a compressed air source, a 3-liter carbon-fiber compact air bottle is assembled on the floating platform. The choice of carbon-fiber material for the compact air bottle is to minimize the weight that the floating platform carries. Therefore, the most important selection criteria for compact air bottles are weight and volume. Moreover, the floating platform can also be used as integrated directly into the high-pressure compressed air system given in Fig. 9. The high-pressure compressed air system is installed outside of Zero-G Lab. However, it has a direct connection inside the lab through the wall. The high-pressure compressed air system and its connection inside Zero-G Lab are given in Fig. 4.

The high-pressure compressed air system consists of two pressure bottles, each 30 liters with a maximum 300 bar capacity. They are replaced by a contractor company when they are finished. They are not being filled with compressed air inside Zero-G Lab due to safety reasons. The high-pressure compressed air system can be used for two purposes; 1-Charging the compact air bottles inside Zero-G Lab, and 2-By-passing the compact air bottles, the high-pressure compressed air system can be used as a

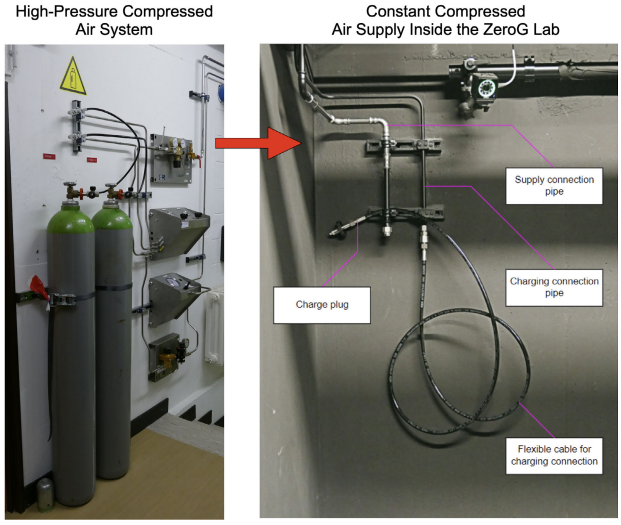

FIGURE 4. The high-pressure compressed air system and its connection inside Zero-G Lab.

compressed air source directly and can be fed to the solenoid valves of the floating platform. In this second case, more experiment time is obtained compared to experiment time using only compact air bottles. The high-pressure compressed air system has an on-board pressure regulator so the on-board pressure regulator has the capability to regulate the pressure from 300 bar to 10 bar since the maximum pressure value for solenoid valves is 10 bar. Depending on the frequency of nozzle usage, the high-pressure compressed air system will endure around 8 hours for actuating one floating platform. Compact air bottles endure around 40 minutes.

5) PRESSURE REGULATION

Pressure regulation is an important process since 300 bar pressure inside the compact air bottle needs to be reduced before the air gets inside the solenoid valve manifold. Therefore, the most important criteria for pressure regulation equipment selection if the input and output pressure value constraints of the equipment. The first step is to reduce the pressure at the output of the compact air bottle to 10 bar. To achieve this, a 300-bar to 10-bar pressure regulator is used as integrated into the compact air bottle. In this study, this pressure regulator is named the main pressure regulator. As a second step regulator, a specific FESTO MS2 pressure regulator is assigned to both air-bearings and nozzles, this condition regulates the pressure values between 0-10 bar for air-bearings and nozzles. The maximum force that can be obtained from a single nozzle is 1 N when the output pressure of the second step pressure regulator is adjusted to 10 bar.

C. ELECTRONIC COMPONENTS

The electronic components of the floating platform are consisting of the driver for solenoid valves, a power source, a voltage regulator, an on-board computer, and sensors.

The basic components of the floating platform are:

1) Driver for solenoid valves: Solenoid valves have simple DC voltage inputs. To energize solenoid valves in a controlled way, a driver board is needed, since the current supply on General Purpose Input-Output (GPIO) pins of RPi4B is limited. The power to drive a single solenoid valve is around 0.3 W. However, GPIO pin of RPi4B is able to give a maximum 16 mA at 3.3 V. To tackle this task, a relay board in Fig. 3 is used as the driver board. GPIO pins of RPi4B simply send low-energy trigger signals to the relay board to actuate the solenoid valves. The relay board is parallelly connected to the 5 V energy supply of the power bank. When it receives a low-energy trigger signal from GPIO pins of RPi4B, it draws the necessary energy from the power bank to actuate the solenoid valves.
2) Power source and voltage regulation: As a power source, a 5 V power bank with 0.27 Ah is used. A voltage regulator is integrated into the output of the power source to regulate the voltage.
3) On-board computer: As an onboard computer, the floating platform has RPi4B that has Quad-core Cortex-A72 (ARM v8) 64-bit 1.5GHz processor with 8GB SDRAM.
4) Motion Capture System (MCS): Six OptiTrack Prime 13W cameras located in Zero-G Lab are used to track the position of the floating platform (at 240 Hz). An active marker is located at the center of the top plate. The position data is processed by the onboard computer. In this paper, only MCS data is used inside the floating platform's closed-loop control.
5) IMU: It is located at the geometric center of the second plate of the floating platform. The sampling frequency of MPU6050 is 1 kHz.
6) Pressure transducer: It measures the pressure inside the compact air bottle and is used to provide data about how long the floating platform can operate. The sampling frequency is 1 kHz.

IV. CONTROLLER DESIGN

We propose to use well-known LMI method to suppress ground-induced mechanical disturbances and make the set-point tracking operations robust against them. A convex optimization-based PD position control approach is applied by minimizing the $\mathcal{H}_2$ norm between the disturbance vector and the controlled output vector. $\mathcal{H}_2$ norm minimization is chosen to suppress the effect of the varying frequency characteristics of the ground-induced mechanical disturbances. A centralized LMI-based controller is assigned to control each DoF. The proposed controller's performance is tested in two experiments. **1-** Position control of a single floating platform, **2-** Cooperative docking, realization of docking scenario by two floating platforms.

A. SYSTEM DYNAMICS

The floating platform with its coordinate system is shown in Fig. 2. In theory, the floating platform freely slides on 2D epoxy floor if a force gradient is applied to it, thus the floating platform is modelled as 3-DoF (two translational DoF and one rotational DoF) free floating object. m is mass of the floating platform, I_z is inertia of yaw axis, F_x is translational force for x axis, F_y is translational force for y axis, T_Θ is torque for z axis, a_x is translational acceleration for x axis, a_y is translational acceleration for y axis, α_z is rotational acceleration for z axis as given in Eq.1.

$$\mathbf{f} = \begin{bmatrix} F_x \\ F_y \\ T_\Theta \end{bmatrix} = \begin{bmatrix} ma_x \\ ma_y \\ I_z\alpha_z \end{bmatrix} \tag{1}$$

The whole dynamics are modelled as LTI (Linear Time Invariant) system due to the following reasons:

- The linear modelling approach brings less computation load to the microprocessor.
- Using linear modelling, less network load is generated during the experiments.

In future studies as extension of this paper, the performance of the nonlinear modelling approach will be compared with the linear modelling approach.

To create the control-loop for the floating platform, parameters to be defined in the state vector have crucial importance. The main reason of this situation is that; the parameters in the state vector will asymptotically converge to a finite value if there will be an optimal and common solution for all the constructed LMIs. To track the desired position and velocity inputs, position and velocity parameters are located in the state vector. The desired position parameters represent the set-points, whereas the desired velocity parameters represent the velocity profile. The state vector is constructed as given in Eq. 2.

$$\mathbf{x} = \begin{bmatrix} \dot{x}_r - \dot{x}_a & x_r - x_a & \dot{y}_r - \dot{y}_a & y_r - y_a & \dot{\Theta}_r - \dot{\Theta}_a & \Theta_r - \Theta_a \end{bmatrix}^T \tag{2}$$

Due to the capability specs of the MCS, the position parameters defined in the state vector are measured at 240 Hz sampling frequency. Taking the derivative of the position data in MCS adds 40 Hz delay. Therefore, the velocity parameters defined in the state vector have 200 Hz sampling frequency. The whole system is modelled in a continuous domain since the data acquisition by the sensory hardware is relatively high.

In application, micron-scale deformation of epoxy floor generates disturbance. The stochastic nature of the mechanical disturbances induced by the epoxy floor for each motion axis are modeled as $\underline{F_x}$, $\underline{F_y}$ and $\underline{T_\Theta}$ in Eq. 3. To avoid/suppress any inclination peak of acceleration, the second derivative of the position references is defined in Eq. 3. Since the magnitude and frequency characteristics of micron-scale deformations of epoxy floor is unknown, $\mathcal{H}_2$ norm between the disturbance vector $\mathbf{w}$ and the controlled output vector $\bar{\mathbf{z}}$

must be minimized for $[0, \infty]$ frequency band.

$$\mathbf{w} = \left[\underline{F_x} \;\; \underline{F_y} \;\; \underline{T_\Theta} \;\; \ddot{x}_r \;\; \ddot{y}_r \;\; \ddot{\Theta}_r \right]^T \tag{3}$$

Any linear time-invariant system can be represented by a state-space framework as given in Eq. 4. The goal is that the parameters defined in the state vector will converge to a finite value while the time goes to infinity under the effect of the disturbance parameters defined in Eq. 3.

$$\frac{\mathbf{dx}}{\mathbf{dt}} = \mathbf{Ax} + \mathbf{B_1 u} + \mathbf{B_2 w} \tag{4}$$

$\mathbf{A} \in \mathbb{R}^{n \times n}$ is the state matrix, $\mathbf{B_1} \in \mathbb{R}^{n \times r}$ is the control input matrix and $\mathbf{B_2} \in \mathbb{R}^{n \times p}$ is the exogenous input matrix which is used to define the effects of external disturbance signals. The control input vector $\mathbf{u} \in \mathbb{R}^r = \mathbf{F}$. $\mathbf{A}$ matrix in Eq. 5, $\mathbf{B_1}$ matrix in Eq. 6 and $\mathbf{B_2}$ matrix in Eq. 7 are constructed to be algebraically compatible with $\mathbf{x}$, $\mathbf{u}$ and $\mathbf{w}$ vectors [40], [41].

$$\mathbf{A} = \begin{bmatrix} 0 & 0 & 0 & 0 & 0 & 0 \\ 1 & 0 & 0 & 0 & 0 & 0 \\ 0 & 0 & 0 & 0 & 0 & 0 \\ 0 & 0 & 1 & 0 & 0 & 0 \\ 0 & 0 & 0 & 0 & 0 & 0 \\ 0 & 0 & 0 & 0 & 1 & 0 \end{bmatrix} \tag{5}$$

$$\mathbf{B_1} = \begin{bmatrix} -1/m & 0 & 0 \\ 0 & 0 & 0 \\ 0 & -1/m & 0 \\ 0 & 0 & 0 \\ 0 & 0 & -1/I \\ 0 & 0 & 0 \end{bmatrix} \tag{6}$$

$$\mathbf{B_2} = \begin{bmatrix} 1/m & 0 & 0 & 1 & 0 & 0 \\ 0 & 0 & 0 & 0 & 0 & 0 \\ 0 & 1/m & 0 & 0 & 1 & 0 \\ 0 & 0 & 0 & 0 & 0 & 0 \\ 0 & 0 & 1/I & 0 & 0 & 1 \\ 0 & 0 & 0 & 0 & 0 & 0 \end{bmatrix} \tag{7}$$

The output vector $\mathbf{y}$ is equal to the state vector $\mathbf{x}$ as shown in Eq. 8.

$$\mathbf{y} = \mathbf{C_1 x} + \mathbf{D_{11} u} + \mathbf{D_{12} w} = \mathbf{x} \tag{8}$$

$\mathbf{C_1} \in \mathbb{R}^{h \times n}$ in Eq. 9, $\mathbf{D_{11}} \in \mathbb{R}^{h \times r}$ in Eq. 10 and $\mathbf{D_{12}} \in \mathbb{R}^{h \times p}$ in Eq. 11 are the measured output matrices with appropriate dimensions.

$$\mathbf{C_1} = \mathbf{I_{6\times 6}} \tag{9}$$

$$\mathbf{D_{11}} = \mathbf{0_{6\times 3}} \tag{10}$$

$$\mathbf{D_{12}} = 0_{6\times 6} \tag{11}$$

Certain output variables are named as the controlled outputs and defined in $\bar{\mathbf{z}} \in \mathbb{R}^m$, which is given by Eq. 12.

$$\bar{\mathbf{z}} = \mathbf{C_2 x} + \mathbf{D_{21} u} + \mathbf{D_{22} w} \tag{12}$$

To minimize the effect of the disturbances defined in the $\mathbf{w}$ vector on all the state parameters, the controlled output matrices are selected to obtain $\bar{\mathbf{z}}$ as the sum of the state parameters as given in Eq. 13, Eq. 14 and Eq. 15.

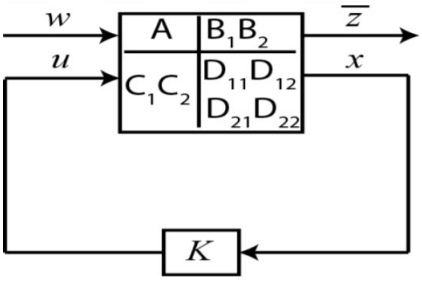

FIGURE 5. General optimal control closed-loop scheme.

$$\mathbf{C_2} = \begin{bmatrix} 1 & 1 & 1 & 1 & 1 & 1 \end{bmatrix} \tag{13}$$

$$\mathbf{D_{21}} = \mathbf{0_{1\times 3}} \tag{14}$$

$$\mathbf{D_{22}} = \mathbf{0_{1\times 6}} \tag{15}$$

$\mathbf{C_2} \in \mathbb{R}^{m \times n}$, $\mathbf{D_{21}} \in \mathbb{R}^{m \times r}$ and $\mathbf{D_{22}} \in \mathbb{R}^{m \times p}$ are the controlled output matrices.

B. $\mathcal{H}_2$ STATE FEEDBACK CONTROLLER SYNTHESIS

For any robustness problem, the main objective is to construct $G_c(s)$ that can minimize the effect of $\mathbf{w}$ parameter on $\bar{\mathbf{z}}$ parameter as shown in Fig. 5.

(i) The closed loop system given in Fig. (5) is asymptotically stable, which indicates that all eigenvalues of $\mathbf{A} + \mathbf{B_1 K}$ have negative real parts (by satisfying Eq. 16 and Eq. 17).

(ii) The effect of the disturbance on the controlled output vector is minimized by minimizing the $\mathcal{H}_2$ norm between the exogenous input vector $\mathbf{w}$, which represents the external mechanical disturbances, and the controlled output vector $\bar{\mathbf{z}}$ (by satisfying Eq. 18).

The following theorem presents a full state feedback $\mathcal{H}_2$ controller design.

Theorem-1 [42]: *For a given positive scalar* r*, the closed loop system given in Eq. (20) is asymptotically stable with* $\mathcal{H}_2$ *norm less than* r*, if there exist positive definite matrices* $\mathbf{Y} \in \mathbb{R}^{n \times n}$ *and* $\mathbf{W} \in \mathbb{R}^{m \times n}$ *subject to the following convex optimization problem.*

$$\min \mathrm{r} \text{ for } ||G_{cl}(s)||_2 < \mathrm{r}; \text{ s.t.Eq.(16), Eq.(18), Eq.(17)}$$

LMI that ensures the stability of the proposed controller is given in Eq. 16.

$$\mathbf{AY} + \mathbf{YA} + \mathbf{B_1 W} + \mathbf{W^T B_1^T} + \mathbf{B_2 B_2^T} < 0 \tag{16}$$

To obtain a solution for Eq.16, there must be a positive definite $\mathbf{Y}$ matrix as shown in Eq. 17.

$$\mathbf{Y} = \mathbf{Y^T} > 0 \tag{17}$$

Minimization of the effect of the mechanical disturbances is possible by minimizing Trace($\mathbf{CYC^T}$) to a finite value, which is r as given in Eq. 18.

$$\mathrm{Trace}(\mathbf{CYC^T}) < \mathrm{r} \;\; \text{for} \;\; \mathrm{r} = ||G||_2^2 \tag{18}$$

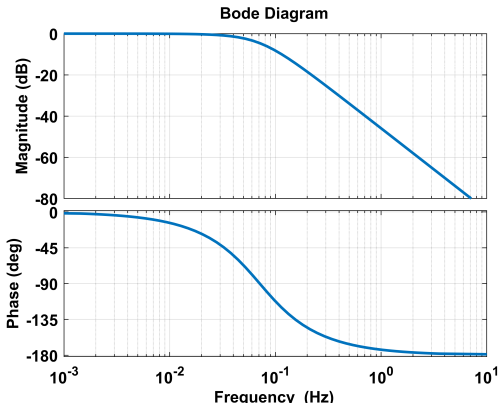

(a) The bode plot of the relation between $\bar{z}$ and $\underline{F_x}$ - $\underline{F_y}$.

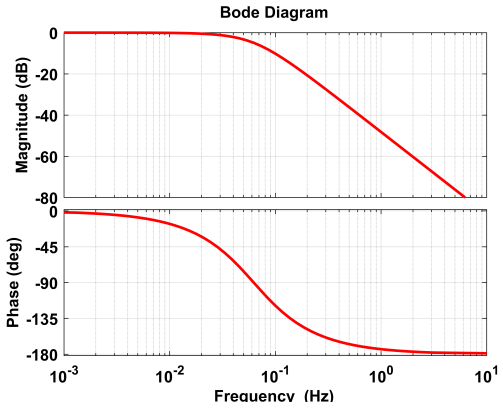

(b) The bode plot of the relation between $\bar{z}$ and $\underline{T_\Theta}$.

FIGURE 6. **The bode plots.**

Then, the resulting K matrix is given in Eq. 19.

$$\mathbf{K} = \mathbf{W}\mathbf{Y}^{-1} \tag{19}$$

By utilizing $\mathbf{K}$ matrix in the closed-loop structure, the resulted closed-loop system is given with Eq. 20 and Eq. 21. Using YALMIP parser and SeDuMi solver, an optimal and common solution that satisfy LMIs in Eq. 16, Eq. 17 and Eq. 18 is calculated. The common solution set of these equations constitutes a convex arena. $\mathbf{K}$ matrix includes PD gains for 3-DoF motion. Therefore, $\mathcal{H}_2$ full state feedback PD gains are computed with Theorem 1. The integral term is not utilized in the controller due to the delay-sensitive nature of the application.

$$\frac{\mathbf{dx}}{\mathbf{dt}} = (\mathbf{A} + \mathbf{B_1}\mathbf{K})\mathbf{x} + \mathbf{B_2}\mathbf{w} \tag{20}$$

$$\bar{\mathbf{z}} = (\mathbf{C_2} + \mathbf{D_{21}}\mathbf{K})\mathbf{x} + \mathbf{D_{22}}\mathbf{w} \tag{21}$$

The synthesized PD gains are placed in $\mathbf{K}$ vector and given in Eq 22. The PD gains defined in $\mathbf{K}$ vector are used to weight the states defined in $\mathbf{x}$ state vector to be used to synthesize the control input vector $\mathbf{u}$ in the closed-loop state feedback

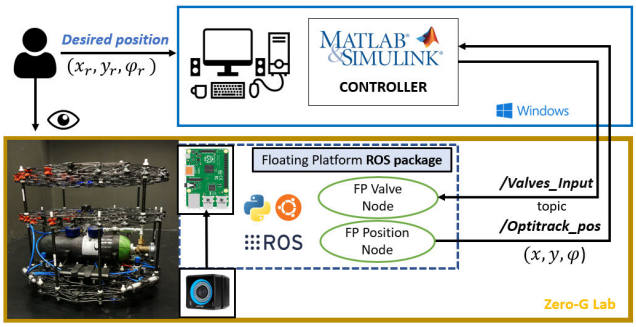

(a) Architecture for real tests.

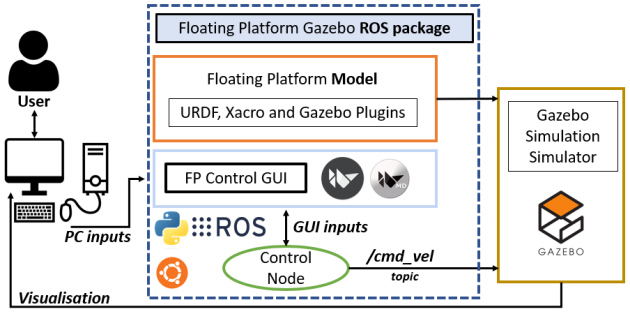

(b) Gazebo simulation.

FIGURE 7. **Software architecture to interface with the real and the simulated floating platform.**

structure.

$$\mathbf{K} = 10^{15}\begin{bmatrix} -0.78 & 0.86 & -0.75 & 0.96 & -2.70 & 0.88 \\ 0.12 & 0.52 & 0.29 & 0.55 & 0.31 & 0.53 \\ 4.40 & 0.36 & 1.69 & 0.18 & 1.96 & 0.31 \end{bmatrix} \tag{22}$$

The resulting closed-loop pole placements that ensure the stability, asymptotic convergence and robustness against disturbances, thus proper set-point tracking performance, are given by Eq. 23.

$$\sigma(\mathbf{A} + \mathbf{B_1}\mathbf{K}) = 10^{14}\begin{bmatrix} -0.7075 \pm 5.3073\mathrm{j} \\ -0.4116 \pm 0.0020\mathrm{j} \\ -0.1200 \pm 0.0040\mathrm{j} \end{bmatrix} \tag{23}$$

C. BODE PLOTS

Bode plots of each motion axis are given in Fig. 6. Because the experimental computation brings computational costs with long-term trial-error experiments being conducted at varying frequencies, the bode plots are obtained by analytical calculations. As can be seen from bode plots, the effect of $\mathbf{w}$ on the controlled output $\bar{\mathbf{z}}$ decreases while the frequency of the disturbance parameters is increasing. The minimized $\mathcal{H}_2$ norms have minimized the magnification band for varying frequency disturbance parameters. The convex optimization method ultimately generates a low-pass filter for the suppression of the disturbance parameters, while it increases set-point tracking performance for constant inputs at low frequencies. Especially after 5×10^{-2} Hz, the controller filters high-frequency disturbances for all DoFs. Since the physical parameters of the floating platform for x and y

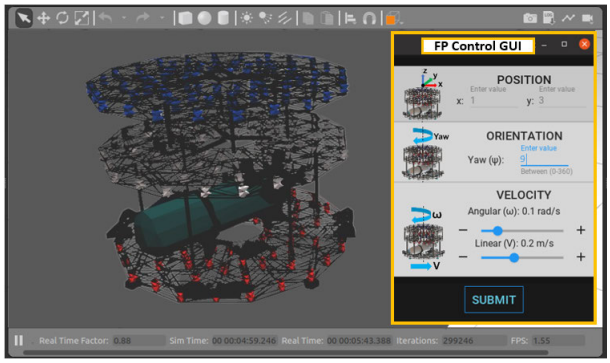

FIGURE 8. 3D Floating platform integrated into Gazebo simulator environment and the control GUI to operate it.

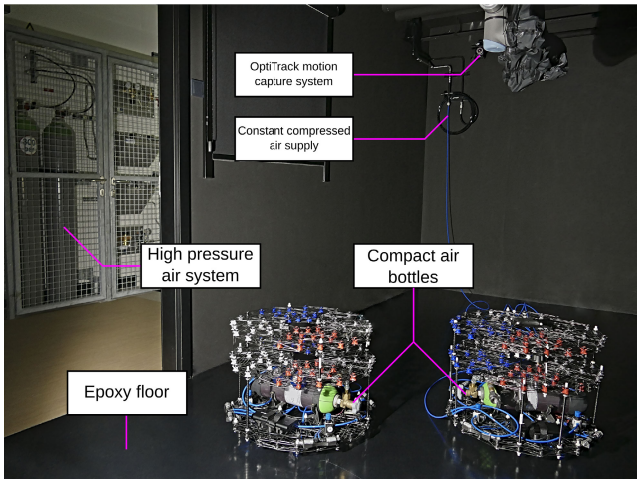

FIGURE 9. SpaceR-SnT's floating platforms inside the Zero-G Lab.

translational axes are identical, they have the same bode plot outputs.

D. MODULATING THE NOZZLE FORCE FROM ANALOG TO DIGITAL

Since the nozzles work with binary logic, signal modulation from analog to digital is needed. To achieve this purpose, PWPF method is utilized [21]. Due to the hardware limitation of the solenoid valves and relay board, the signals are modulated at 1 Hz. PD gains synthesized in Eq. 22 are used as Pulse-Width value in the modulated output signals.

V. SOFTWARE ARCHITECTURE

Two architectures have been created for the floating platform. One is designed for real testing in the Zero-G Lab facility, while the other one is used to simulate the platform's movements in a controlled environment for testing purposes. For more details, both architectures are presented in Fig. 7.

A. FLOATING PLATFORM SOFTWARE

The software developed has been designed with agile and flexible capabilities to control the floating platform in the Zero-G Lab. The software is divided into two parts,

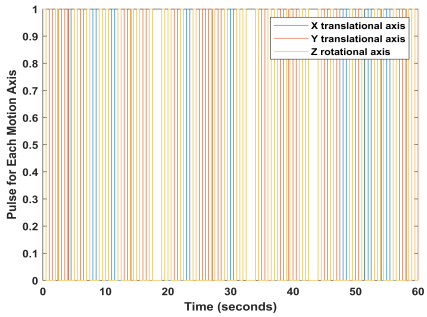

(a) Pulse of each DoF while set-point reference is zero.

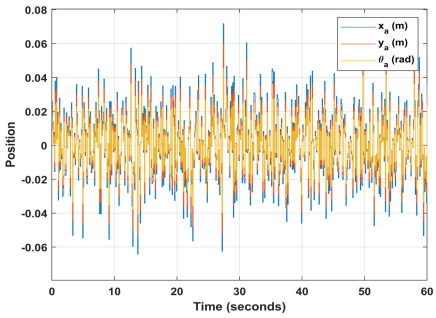

(b) Position change of each DoF for set-point reference is zero.

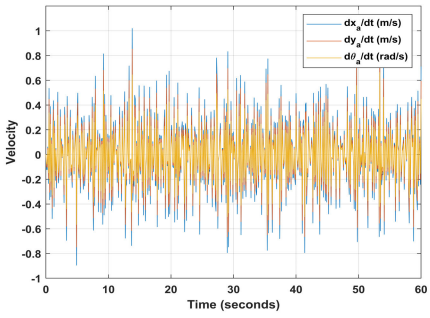

(c) Velocity change of each DoF for set-point reference is zero.

FIGURE 10. The experiment data when set-point reference is zero.

as shown in Fig. 7a. The first part is the controller PC with Windows 10 OS (Operating System). It runs MATLAB and Simulink. It contains the controller explained in Section V, which calculates the status of the eight valves (open or close) based on the desired position (manually set x_r, y_r, ψ_r), and the floating platform real position (x, y, ψ). The latter is received from the MCS of the Zero-G lab through the floating platform RPi v4B.

The other part of the software contains the Floating Platform ROS package. It runs on the RPi v4B computational unit embedded on the floating platform under the Ubuntu OS 20.04. The ROS package receives the status of the valves (/valves_input topic) information from MATLAB and Simulink using the ROS toolbox, an interface that enables connectivity between them. Thereby, the ROS package has the functionality to directly control the floating platform's valves, wherein the solenoid valve has an optimal frequency

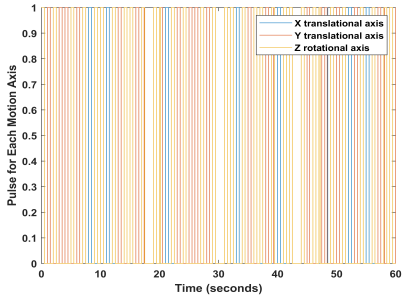

(a) Pulse of each DoF while set-point reference is from point A to B.

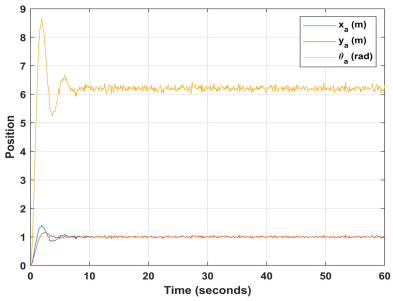

(b) Position change of each DoF for set-point reference is from point A to B.

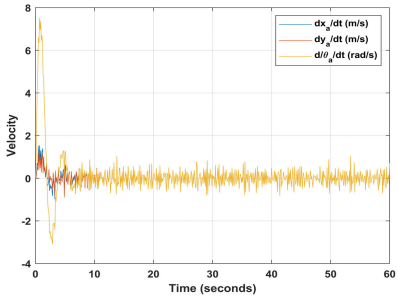

(c) Velocity change of each DoF for set-point reference is from point A to B.

FIGURE 11. The experiment data when set-point reference is from point A to B.

of actuation at 5 Hz and a maximal frequency of actuation at 10 Hz. In addition, the ROS package also processes the positions captured by the Optitrack system by means of the vrpn package, sending the topic /optitrack_pos with the 3D position data of the floating platform's MCS marker.

The advantage of this ROS package is that it enables real-time operation, configurable performance profiles, and backward and forward compatibility provided through Docker integration in the ROS middleware used with custom-developed packages. It provides different ROS versions' compatibility, guaranteeing its repeatability and portability. The software has also been integrated into an outer CI/CD pipeline using Docker. It ensures that any changes to the code are automatically built, tested, and deployed to the floating platform. Also, it provides a personalized infrastructure for floating platform deployment with the ability to support a variety of use cases. For example, the user has the possibility

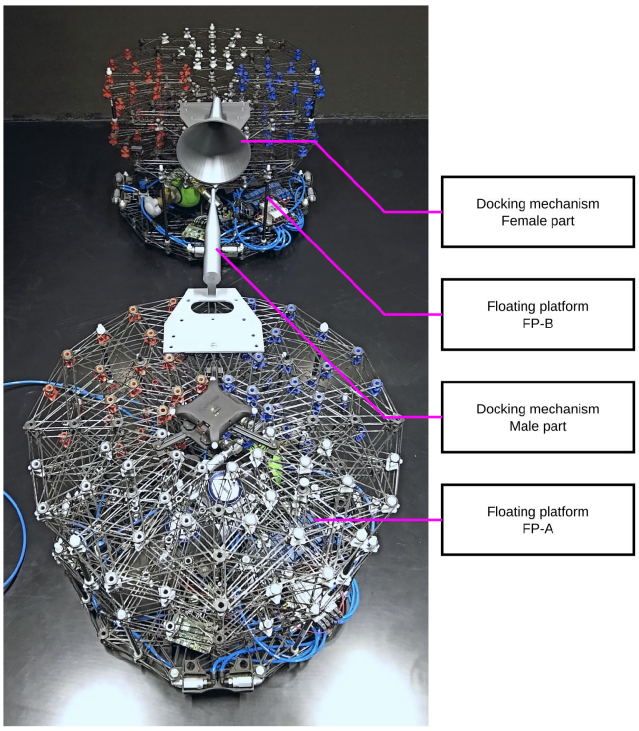

FIGURE 12. Docking experiment.

to integrate any control algorithm using the open-source package given in [Appendix-B].

B. FLOATING PLATFORM SIMULATOR

Simulators offer a risk-free and cost-effective way for users to experiment and analyze the movements and behavior of robotic systems. This work has developed a simulation environment that allows users to interact with a 3D floating platform model using a GUI, as depicted in Fig. 8.

We have configured the Gazebo ROS package with the following physical parameters: total weight 10.95 kg, radius 30 cm, height 60 cm and the inertial values $I_{xx} = 9.72$ kgm^2, $I_{yy} = 9.72$ kgm^2 (due to the symmetry) and $I_{zz} = 7.52$ kgm^2. The friction coefficient can be defined by the user to model the characteristics of different epoxy floors.

The software architecture and interfaces, illustrated in Fig. 7b, utilize ROS as the framework for controlling the floating platform in the Gazebo simulator environment on a Ubuntu OS 20.04, using Python 3. The software architecture is based on a client-server model, in which the server provides services to control the platform in the simulated environment, and the client interacts with it through the control GUI.

- The control GUI showed in Fig. 8. allows the operator to insert set the desired position (x, y), orientation (ψ), angular velocity (ω), and linear velocity (υ) of the floating platform in the simulator, as Fig. 8 shows. They are represented in Eq. 2 with the following nomenclature: $x \rightarrow x_r$, $y \rightarrow y_r$, $\psi \rightarrow \Theta_r$, $\omega \rightarrow \dot{\Theta}_r$, $v \rightarrow \dot{x}_a + \dot{y}_r$

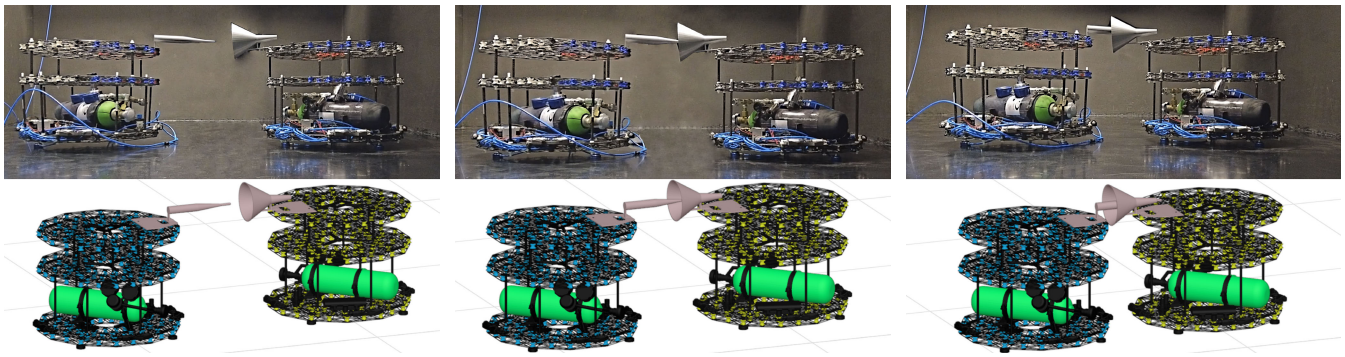

(a) Starting state (b) Approaching state (c) Docking state

FIGURE 13. States of the docking procedure experiment.

- The ROS control node acts as an interface between the user and the Gazebo simulation. It is responsible for launching the GUI, receiving user data, and calculating the linear and angular velocities along the three axes needed to reach the desired position, giving /cmd_vel commands as output to move the floating platform.
- The 3D floating platform model is configured in the floating platform simulation package to be visualized and managed in Gazebo. The Gazebo simulator visually represents the floating platform behavior according to the /cmd_vel topic and ROS model configuration.

The modular approach of the presented ROS package has a clear advantage, as it allows easy integration of new features. For example, different types of position or velocity controllers can be easily incorporated, as well as the addition of new physical parameters relevant to the simulation world. It makes the software highly scalable and adaptable, facilitating future research and applications.

VI. EXPERIMENTAL RESULTS

A. EXPERIMENTAL SETUP

The floating platform and its proposed position controller are tested in the ZeroG-Lab facility of the University of Luxembourg, in two scenarios: 1) Set-point tracking (zero and non-zero values), and 2) Emulation of an on-orbit scenario.

As shown in Fig. 9, the facility is a 5m x 3m area. The facility has four main components to emulate on-orbit scenarios: a Sun emulator to recreate the challenging space lighting conditions, a 240 Hz sampling rate advanced MCS to provide ground truth data, two UR10e robotic manipulators, and two floating platforms to emulate microgravity conditions. The robots, the floating platforms, the MCS, as well as other external devices, communicate and are controlled using ROS.

The controller is modeled in MATLAB-Simulink. External commands to control the floating platform are directed over the ROS network of the ZeroG-Lab. During the experiments, the calculated network ping is approximately 50 ms. The feedback loop is closed using the position data provided by the MCS. In MATLAB-Simulink, a Variable-Step solver is utilized due to its performance in dealing with potential delays in the network. EKF (Extended Kalman Filter) is used to deal with the noise in the MCS feedback data [22]. The experiment results contain steady-state responses even though the nature of the disturbance and noise make the results look as if they contain transient responses.

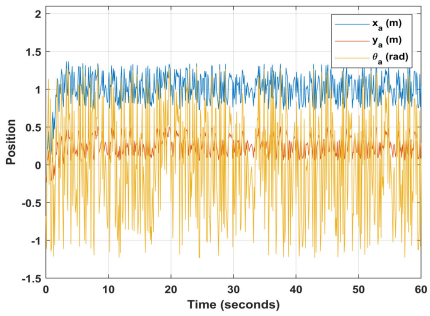

(a) Position change of each DoF of FP-A during the docking.

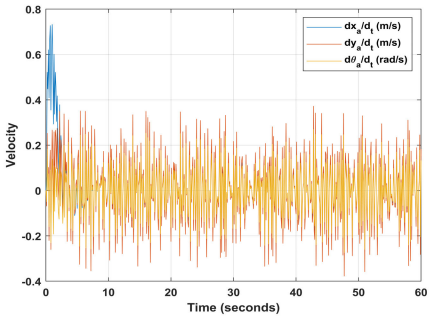

(b) Velocity change of each DoF of FP-A during the docking.

FIGURE 14. The experiment data of FP-A for the docking scenario.

B. SET-POINT TRACKING

To show the asymptotic convergence and stability aspects of the controller, the duration of the experiments is chosen as 60 seconds. Within this section, pulse, position, and velocity

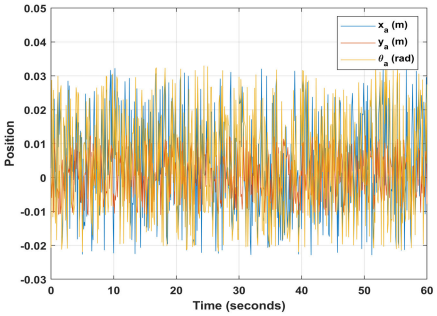

(a) Position change of each DoF of FP-B during the docking.

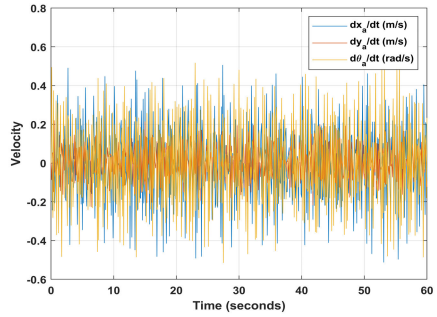

(b) Velocity change of each DoF of FP-B during the docking.

FIGURE 15. The experiment data of FP-B for the docking scenario.

plots are given. Since pulse data is identical to force data and nozzles are working in binary logic, force plots are not given. For x and y translational axes, the total force is 2 N when two related nozzles are actuated. For z (yaw) rotational axis, total torque is 2 N $\times$ 0.3 m when two related nozzles are actuated.

1) ZERO SET-POINT SCENARIO

In this experiment, the centralized controller is used with the reference set-point parameters $x_r = 0$, $y_r = 0$, and $\Theta_r = 0$.

The experiment's results are given in Fig. 10. In Fig. 10a, the pulse of each DoF while set-point reference is zero can be seen. In Fig. 10, it can be observed that x_a, y_a, and Θ_a parameters oscillate around the desired reference set-point, which is zero. In Fig. 10c, it is shown that the velocity parameters have oscillation behavior around zero as well.

2) NON-ZERO SET-POINT SCENARIO

In the set-point tracking experiment, the centralized controller has been used with the reference set-point parameters $x_r = 1$ m, $y_r = 1$ m, and $\Theta_r = 2\pi$ rad. The experiment's results are given in Fig. 11. In Fig. 11a, the pulse of each DoF while set-point reference is non-zero can be seen. In Fig. 11b, it can be seen that x_a and y_a parameters oscillate around their desired reference set-point, which is 1, and Θ_a oscillates around its desired set-point 2π. In Fig. 11c, it is shown that the velocity parameters converge to zero after overshoot.

C. EMULATION OF ON-ORBIT DOCKING SCENARIO

The docking experiment setup can be seen in Fig. 12. The set-points for the docking experiment are determined by considering the proper alignment between male and female docking parts. The docking experiments are conducted in a cooperative approach, which means that we have the position data of both FP-A and FP-B. The docking experiment's states are given in Fig. 13, (a) Starting state, (b) Approaching state, and (c) Docking state. The first raw shows the Zero-G Lab environment and the second raw shows the Gazebo simulation. The simulation results are not given since the simulation does not include uncertain dynamics of the epoxy floor. The reference set-point for FP-A is $x_r = 1$ m, $y_r = 0.4$ m and $\Theta_r = 0$ rad, and the reference set-point for FP-B is $x_r = 0$, $y_r = 0$ and $\Theta_r = 0$. To achieve the cooperative docking experiment, the controller of FP-A tracks the given set-point, while the controller of FP-B works for zero set-point tracking to stay steady. The position and velocity values of FP-A are given in Fig. 14a and Fig. 14b, whereas the position and velocity values of FP-B are given in Fig. 14c and Fig. 14d. As can be seen from these figures, the position parameters asymptotically converge to the desired set-points while the velocity parameters asymptotically converge to zero for each DoF. During these experiments; stability, asymptotic convergence, disturbance rejection and reference trajectory tracking of desired position goals are met. Two floating platforms dock successfully.

VII. CONCLUSION

In this paper, we firstly presented a novel lightweight floating platform structure made from additive manufacturing using carbon-fibre material. Secondly, the software packages based on ROS were given, the ROS packages were provided as open source for researchers of the orbital robotics community, allowing them to simulate/experiment with their control approaches. Thirdly, a disturbance rejection-based closed-loop position control strategy for orbital scenario emulation was applied. The synthesized LMIs were capable of disturbance rejection and set-point tracking problems at the same time. The effectiveness of this control approach was shown in two scenarios: the position control of a single floating platform and the position control of two floating platforms in a cooperative docking scenario. LMIs were constructed to satisfy $\mathcal{H}_2$ norm minimization property to suppress the epoxy floor-induced mechanical disturbances. Based on the numeric results obtained during the experiments, we validated that the proposed floating platform can be used for the emulation of on-orbit scenarios. The future works will focus on various reinforcement learning methods to suppress ground-induced mechanical disturbances.

APPENDIX-A

General overview video of Zero-G Lab, ''The Zero-G Lab: Testing in Micro-Gravity Environment'', can be watched from this link. The docking experiment video can be downloaded from this link.

APPENDIX-B

ROS packages can be downloaded from this link.

ACKNOWLEDGMENT

The national patent application in Luxembourg "Pneumatic floating systems for performing zero-gravity experiments" has been filed and it is still under evaluation process, file number: LU503146. As next step, TTO of SnT is preparing to submit an international patent. SpaceR's official webpage https://www.spacer.lu/.

REFERENCES

[1] J. Chatterjee, J. N. Pelton, and F. Allahdadi, "Active orbital debris removal and the sustainability of space," in *Handbook of Cosmic Hazards and Planetary Defense*. Cham, Switzerland: Springer, 2015, pp. 921–940.

[2] T. Rybus and K. Seweryn, "Planar air-bearing microgravity simulators: Review of applications, existing solutions and design parameters," *Acta Astronaut.*, vol. 120, pp. 239–259, Mar. 2016.

[3] H. Kolvenbach and K. Wormnes, "Recent developments on orbit, a 3-DoF free floating contact dynamics testbed," in *Proc. Int. Symp. Artif. Intell., Robot. Automat. Space (i-SAIRAS)*, Beijing, China, Jun. 2016, pp. 1–7.

[4] M. Zwick, I. Huertas, L. Gerdes, and G. Ortega, "ORGL—ESA's test facility for approach and contact operations in orbital and planetary environments," in *Proc. 14th Int. Symp. Artif. Intell., Robot. Automat. Space (i-SAIRAS)*, Madrid, Spain, Jun. 2018, pp. 1–7.

[5] M. Wilde, B. Kaplinger, T. Go, H. Gutierrez, and D. Kirk, "Orion: A simulation environment for spacecraft formation flight, capture, and orbital robotics," in *Proc. IEEE Aerosp. Conf. (AEROCONF)*, Big Sky, MT, USA, Mar. 2016, pp. 1–14.

[6] P. Tsiotras, "ASTROS: A 5DOF experimental facility for research in space proximity operations," in *Proc. AAS Guid. Control Conf.*, vol. 114, 2014, pp. 1–14.

[7] D. Gallardo, R. Bevilacqua, and R. Rasmussen, "Advances on a 6 degrees of freedom testbed for autonomous satellites operations," in *Proc. AIAA Guid., Navigat., Control Conf.*, Aug. 2011, p. 6591.

[8] J. L. Schwartz, M. A. Peck, and C. D. Hall, "Historical review of air-bearing spacecraft simulators," *J. Guid., Control, Dyn.*, vol. 26, no. 4, pp. 513–522, Jul. 2003.

[9] W. F. R. Ribeiro, K. Uno, M. Imai, K. Murase, B. Can Yalçın, M. E. Hariry, M. A. Olivares-Mendez, and K. Yoshida, "Mobility strategy of multi-limbed climbing robots for asteroid exploration," 2023, *arXiv:2306.07688*.

[10] C. Menon, A. Aboudan, S. Cocuzza, A. Bulgarelli, and F. Angrilli, "Free-flying robot tested on parabolic flights: Kinematic control," *J. Guid., Control, Dyn.*, vol. 28, no. 4, pp. 623–630, Jul. 2005.

[11] B. C. Yalcin, C. Martinez, S. Coloma, E. Skrzypczyk, and M. O. Mendez, "Ultra-light floating platform: An orbital emulator for space applications," in *Proc. IEEE Int. Conf. Robot. Automat. (ICRA)*, May 2023.

[12] V. Muralidharan, M. R. Makhdoomi, K. R. Barad, M. Amaya, M. Lina, K. C. Howell, C. M. Luna, and M. A. O. Mendez, "Hardware-in-the-loop proximity operations in cislunar space," in *Proc. Int. Astron. Congr. (IAC)*, 2022, p. 15.

[13] M. R. Makhdoomi, V. Muralidharan, K. R. Barad, J. Sandoval, M. Olivares-Mendez, and C. Martinez, "Emulating on-orbit interactions using forward dynamics based Cartesian motion," 2022, *arXiv:2209.15406*.

[14] E. Papadopoulos, I. Paraskevas, T. Flessa, K. Nanos, Y. Rekleitis, and I. Kontolatis, "The NTUA space robot simulator: Design and results," in *Proc. 10th ESA Workshop Adv. Space Technol. Robot. Automat.*, Nov. 2018. [Online]. Available: https://www.esa.int/Enabling_Support/Space_Engineering_Technology/Automation_and_Robotics/Proceedings_of_ASTRA

[15] O. Jakub, J. Kindracki, T. Rybus, Ł. Mężyk, P. Paszkiewicz, R. Moczydłowski, T. Barciński, K. Seweryn, and P. Wolański, "2D microgravity test-bed for the validation of space robot control algorithms," *J. Autom., Mobile Robot. Intell. Syst.*, vol. 11, no. 2, pp. 95–104, Jun. 2017.

[16] M. Schlotterer and S. Theil, "Testbed for on-orbit servicing and formation flying dynamics emulation," in *Proc. AIAA Guid., Navigat., Control Conf.*, Toronto, ON, Canada, Aug. 2010.

[17] K. Yoshida, "Experimental study on the dynamics and control of a space robot with experimental free-floating robot satellite," *Adv. Robot.*, vol. 9, no. 6, pp. 583–602, Jan. 1994.

[18] E. Papadopoulos, F. Aghili, O. Ma, and R. Lampariello, "Robotic manipulation and capture in space: A survey," *Frontiers Robot. AI*, vol. 8, p. 228, Jul. 2021.

[19] K. Yoshida, "ETS-VII flight experiments for space robot dynamics and control," in *Experimental Robotics VII*, D. Rus and S. Singh, Eds. Berlin, Germany: Springer, 2001, pp. 209–218.

[20] J. D. Mitchell, S. P. Cryan, D. Strack, L. L. Brewster, M. J. Williamson, R. T. Howard, and A. S. Johnston, "Automated rendezvous and docking sensor testing at the flight robotics laboratory," in *Proc. IEEE Aerosp. Conf.*, Mar. 2007, pp. 1–16.

[21] A. Bredenbeck, S. Vyas, M. Zwick, D. Borrmann, M. A. Olivares-Mendez, and A. Nüchter, "Trajectory optimization and following for a three degrees of freedom overactuated floating platform," in *Proc. IEEE/RSJ Int. Conf. Intell. Robots Syst. (IROS)*, Kyoto, Japan, Oct. 2022, pp. 4084–4091.

[22] C. K. Chui and G. Chen, *Kalman Filtering With Real-Time Applications* (Springer Series in Information Sciences), vol. 17. Springer, 1987.

[23] A. Redah, T. Mikschl, and S. Montenegro, "Physically distributed control and swarm intelligence for space applications," in *Proc. 14th Int. Symp. Artif. Intell., Robot. Automat. Space (i-SAIRAS)*, Madrid, Spain, Jun. 2018, pp. 1–6.

[24] A. Redah, H. R. Ramavaram, and S. Montenegro, "Robotic testing platform for autonomous rendezvous and docking of floating vehicles," in *Proc. 11th Int. Symp. Artif. Intell., Robot. Automat. Space (i-SAIRAS)*, Turin, Italy, Sep. 2012, pp. 1–7.

[25] S. Wehrmann and M. Schlotterer, "Coordinated orbit and attitude control of a satellite formation in a satellite simulator testbed," in *Proc. ESA GNC*, Salzburg, Austria, May/Jun. 2017.

[26] R. Zappulla, J. Virgili-Llop, C. Zagaris, H. Park, and M. Romano, "Dynamic air-bearing hardware-in-the-loop testbed to experimentally evaluate autonomous spacecraft proximity maneuvers," *J. Spacecraft Rockets*, vol. 54, no. 4, pp. 825–839, Jul. 2017.

[27] R. Bevilacqua, T. Lehmann, and M. Romano, "Development and experimentation of LQR/APF guidance and control for autonomous proximity maneuvers of multiple spacecraft," *Acta Astronaut.*, vol. 68, nos. 7–8, pp. 1260–1275, Apr. 2011.

[28] M. Sabatini, M. Farnocchia, and G. B. Palmerini, "Design and tests of a frictionless 2D platform for studying space navigation and control subsystems," in *Proc. IEEE Aerosp. Conf.*, Mar. 2012, pp. 1–12.

[29] M. Sabatini, P. Gasbarri, and G. B. Palmerini, "Design, realization and characterization of a free-floating platform for flexible satellite control experiments," *Acta Astronaut.*, vol. 210, pp. 576–588, Sep. 2023.

[30] A. A. Pothen, A. Crain, and S. Ulrich, "Pose tracking control for spacecraft proximity operations using the Udwadia–Kalaba framework," *J. Guid., Control, Dyn.*, vol. 45, no. 2, pp. 296–309, 2022.

[31] A. Banerjee, S. G. Satpute, C. Kanellakis, I. Tevetzidis, J. Haluska, P. Bodin, and G. Nikolakopoulos, "On the design, modeling and experimental verification of a floating satellite platform," *IEEE Robot. Autom. Lett.*, vol. 7, no. 2, pp. 1364–1371, Apr. 2022.

[32] Y. K. Nakka and S.-J. Chung, "Trajectory optimization of chance-constrained nonlinear stochastic systems for motion planning under uncertainty," *IEEE Trans. Robot.*, vol. 39, no. 1, pp. 203–222, Feb. 2023.

[33] Y. Nesterov and A. Nemirovskii, *Interior-Point Polynomial Algorithms in Convex Programming*. Philadelphia, PA, USA: Society for Industrial and Applied Mathematics, 1994.

[34] J. F. Sturm, "Using SeDuMi 1.02, a MATLAB toolbox for optimization over symmetric cones," *Optim. Methods Softw.*, vol. 11, nos. 1–4, pp. 625–653, Jan. 1999.

[35] J. Lofberg, "YALMIP: A toolbox for modeling and optimization in MATLAB," in *Proc. IEEE Int. Conf. Robot. Autom.*, Sep. 2004, pp. 284–289.

[36] A. R. Parkinson, R. Balling, and J. D. Hedengren, *Optimization Methods for Engineering Design*, 2nd ed. Provo, UT, USA: Brigham Young Univ., 2018.

[37] R. Crowther, "Space junk-protecting space for future generations," *Science*, vol. 296, no. 5571, pp. 1241–1242, May 2002.

[38] D. Mehrholz, L. Leushacke, W. Flury, R. Jehn, H. Klinkrad, and M. Landgraf, "Detecting, tracking and imaging space debris," *ESA Bull.*, no. 109, pp. 128–134, 2002.

[39] R. Zappulla, "Experimental evaluation methodology for spacecraft proximity maneuvers in a dynamic environment," Ph.D. thesis, Naval Postgraduate School, Monterey, CA, USA, 2017.
[40] K. Zhou, J. C. Doyle, and K. Glover, *Robust and Optimal Control*, 1st ed. London, U.K.: Pearson, Aug. 1995.
[41] G. E. Dullerud and F. Paganini, *A Course in Robust Control Theory: A Convex Approach*. New York, NY, USA: Springer, Mar. 2013.
[42] S. Boyd, L. E. Ghaoui, E. Feron, and V. Balakrishnan, *Linear Matrix Inequalities in System and Control Theory*. Philadelphia, PA, USA: Society for Industrial and Applied Mathematics, 1994.

BARIŞ CAN YALÇIN (Member, IEEE) received the Ph.D. degree from the Mechatronics Engineering Department, Yildiz Technical University, Turkey, in 2019. He gained working experience with Yildiz Technical University, as a Research and Teaching Assistant. During his Ph.D., he studied on the control theory topics and worked to design a novel control method to suppress micron-scale vibrations using magnetic levitation technology. He is currently with the Space Robotics Research Group (SpaceR), SnT, University of Luxembourg, headed by Prof. Miguel Angel Olivares Mendez, as a Research Associate/Postdoctoral Researcher. He is researching space mechatronics domain to create various space related mechatronic systems, such as floating platforms and active/passive space debris removal systems. He is a Designer of SpaceR, SnT's floating platform. He uses the floating platform for several research domains, such as close proximity, rendezvous, asteroid/planetary landing, and locomotion scenarios. In SpaceR, he contributes to ESA and FNR funded projects in which the floating platform plays a crucial role in realizing orbital robotic scenarios.

CAROL MARTINEZ (Member, IEEE) received the M.Sc. and Ph.D. degrees in robotics and automation from Universidad Politécnica de Madrid (UPM), in 2009 and 2013, respectively, with a focus on computer vision for unmanned aerial vehicles (visual tracking, pose estimation, and control), for which she received the outstanding Ph.D. thesis award by UPM. As a Ph.D. candidate, she was a Visiting Researcher with the Queensland University of Technology and the University of Bristol, U.K., where she developed algorithms for tracking and pose estimation using cameras on-board aerial vehicles. She held positions as a Postdoctoral Researcher with UPM, and an Assistant Professor with PUJ, Bogotá, Colombia, from 2015 to 2020. She has led and conducted interdisciplinary research in computer vision, machine learning, and deep learning for process automation (industry and health) and robotics (aerial, industrial, and space). Since 2020, she has been a Research Scientist with SnT, Space Robotics Research Group, University of Luxembourg (UniLu), where she leads projects in orbital robotics (space debris removal and vision-based navigation), robotic manipulation (control, perception, and learning), and on-ground testing environment (ZeroGLab facility). She is currently a Lecturer of the Interdisciplinary Space Master (ISM) Program with UniLu and provides guidance and supervision to master's and Ph.D. Researchers (as a Co and a Main supervisor). She is a Mechatronics Engineer with UPM. Her research interests include perception approaches for the autonomous operation of robots in space and multi-purpose manipulation tasks for planetary and orbital robotics applications.

SOFÍA COLOMA received the bachelor's degree in automation and industrial electronics engineering, in 2014, the M.Sc. degree in robotics and automation, in 2015, the Ph.D. degree in robotics and automation from Universidad Politécnica de Madrid (UPM), Spain, in 2020, and the M.Sc. degree in artificial intelligence and data science, in 2021. She completed internships with the German Aerospace Center (DLR) and the European Organization for Nuclear Research (CERN). From 2015 to 2021, she developed her professional career with the Center for Automation and Robotics (CAR), UPM-CSIC, working on important and unique projects, such as the Demo-Oriented Neutron Source (DONES) particle accelerator. She is currently a Postdoctoral Researcher with the Space Robotics Group, SnT, University of Luxembourg. Her research interests and experience have been focused on telerobotics, especially in hostile and challenging environments. Her research interests include robotics control, extended reality, artificial intelligence, and data science to be applied to planetary robotics.

ERNEST SKRZYPCZYK received the dual master's degree from the University of Genova, Italy, and Centrale Nantes, France, in 2017. He gained research and development experience working in the industry and independently, mostly in the area of computer vision and perception. He has expertise on GNU/Linux. He is currently a Research and Development Specialist with SpaceR.

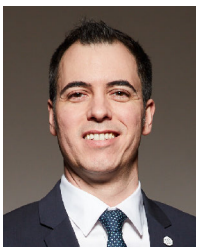

MIGUEL A. OLIVARES-MENDEZ (Member, IEEE) received the Engineering degree in computer science from the University of Malaga, in 2006, and the M.Sc. and Ph.D. degrees in robotics and automation from the Technical University of Madrid, in 2009 and 2013, respectively.

During his Ph.D., he was a Visiting Researcher with EPFL, Switzerland, and ARCAA-QUT, Australia. In May 2013, he joined the Interdisciplinary Centre for Security Reliability and Trust (SnT), University of Luxembourg (Uni.Lu), as an Associate Researcher with the Automation and Robotics Research Group. In December 2016, he became a Research Scientist and is the main responsible of the research activities on mobiles robotics with the Automation and Robotics Research Group, SnT, Uni.Lu. He is currently a tenured Assistant Professor of space robotics and a Senior Research Scientist with the Interdisciplinary Centre for Security, Reliability and Trust, University of Luxembourg. He leads the Space Robotics Research Group (SpaceR), LunaLab, and the Zero-Gravity Laboratory. He is also a main supervisor of 11 Ph.D. students and seven Postdocs. He has published more than 120 peer-reviewed publications. His research interests include aerial, planetary and orbital robotics for autonomous navigation, situational awareness, perception, machine learning, multi-robot interaction in autonomous exploration, inspection, and operations.

Dr. Olivares-Mendez is an Associate Editor of IROS, ICRA, and ICUAS conferences; and the *Journal of Intelligent and Robotics Systems*, *Frontiers on Space and Field Robotics*, and *The International Journal of Robotics Research* (IJRR).